

Chapter 3

Direct Numerical Simulation

3.1 Introduction

For the computation of the POD we need a large database of snapshots. These snapshots can be supplied by either experiment or numerical simulation (or both). In our case the snapshots are supplied by a direct numerical simulation (DNS).

In the following chapters we compute POD's of 2D and 3D driven cavity flows. For this purpose 2D and 3D DNS have been performed. The 2D DNS of the driven cavity uses a Reynolds number of $Re=22,000$ for the building of the database for the POD. We have chosen $Re=22,000$ because at this Reynolds number this flow is turbulent, as we know from previous simulations (see [62, 57, 56]).

3D computations have shown that the 3D driven cavity is already unstable at $Re=3,200$. This means that the 2D solution, which has a stable steady solution till approximately $Re=10,000$, is not a physical solution. Therefore for real turbulence we need to do a 3D simulation.

The 3D DNS has been done at $Re=10,000$. At this Reynolds number a turbulent solution exists, and experimental data is available (see [42]) for comparison. Results of the DNS agreed well with the experimental data (see [58]).

This chapter consists of 2 sections. In Section 3.2 we present results of the 2D DNS, and describe the database for the 2D POD. In Section 3.3 the 3D DNS is presented.

3.2 2D DNS

3.2.1 Numerical method

The geometry and boundary conditions of the the 2D driven cavity are shown in Fig. 3.1. In this geometry the incompressible Navier-Stokes equations (in conservative form)

$$\begin{aligned}\nabla \cdot \mathbf{u} &= 0 \\ \frac{\partial \mathbf{u}}{\partial t} + \nabla \cdot (\mathbf{u}\mathbf{u}) &= -\nabla p + \frac{1}{Re} \Delta \mathbf{u}\end{aligned}\tag{3.1}$$

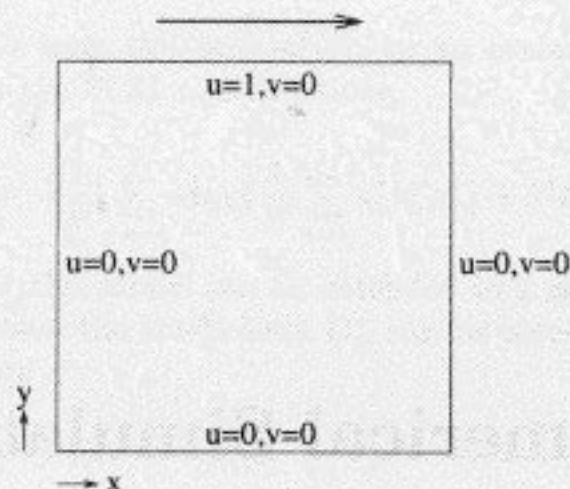


Figure 3.1: *Geometry of the 2D driven cavity with boundary conditions. The cavity is of unit length and width.*

are solved. The grids on which the equations are solved vary from 250×250 to 500×500 with uniform and slightly stretched cell-widths. The unknowns are staggered. The numerical method which is used is based on the Marker-and-Cell method [25]. The pressure gradient and the incompressibility constraint are treated implicitly; the convective and viscous terms are treated explicitly. The spatial discretizations are second-order accurate. Also a fourth-order accurate space discretization has been used. This fourth-order accuracy is achieved by a Richardson extrapolation of the second-order accurate spatial discretization (see [59]).

The discrete Poisson equation for the pressure is solved using the conjugate gradient method with modified incomplete Choleski preconditioning. The ICCG code is fully vectorized by explicitly reordering the unknowns along diagonals of the grid, and is optimized using Eisenstat's implementation (cf. [17] and references therein). The CPU time of the code is $2.4 \mu\text{s}$ per grid-point per time step on the one-processor CRAY Y-MP.



Figure 3.2: *Streamlines of the computed flow in the 2D driven cavity at $Re=6,000$.*

3.2.2 Solutions for various Reynolds numbers

The 2D driven cavity is a well known test problem. Often Ghia et al. [20] is taken as a reference for 2D driven cavity solutions up to $Re=10,000$. They found steady-state solutions up to and including $Re=10,000$. Our DNS computations show that the first Hopf bifurcation takes place at approximately $Re=7,972$. A second Hopf bifurcation has taken place before $Re=10,000$.

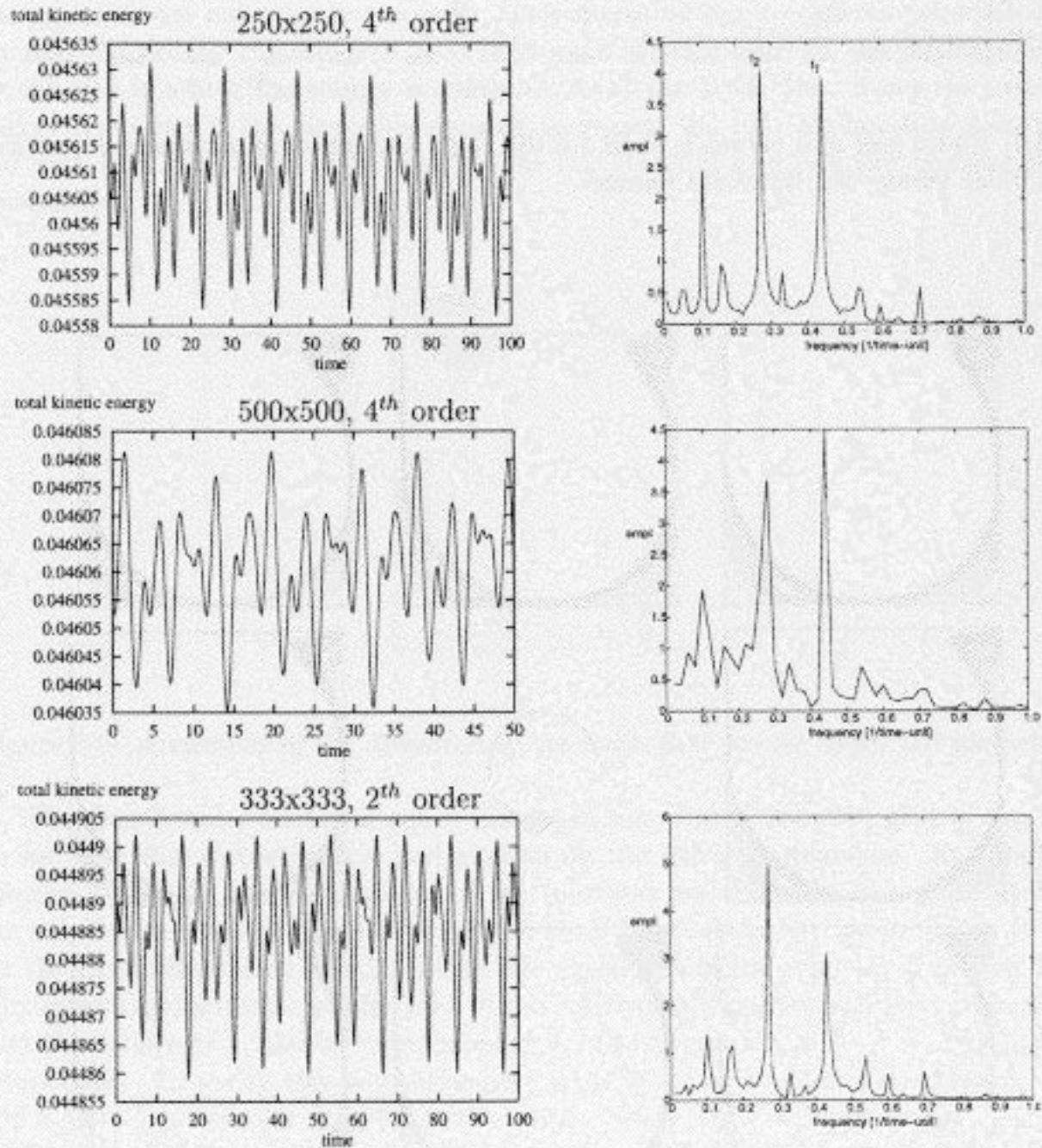


Figure 3.3: Time-series of the total energy (left) and amplitude spectrum (right) of 3 different simulations at $Re=10,000$. The time-series of the middle plot is only 50 time units long, whereas the others are 100 time units long. The time $t=0$ has been set arbitrary. All solutions are 2-periodic with approximately the same two frequencies f_1 and f_2 .

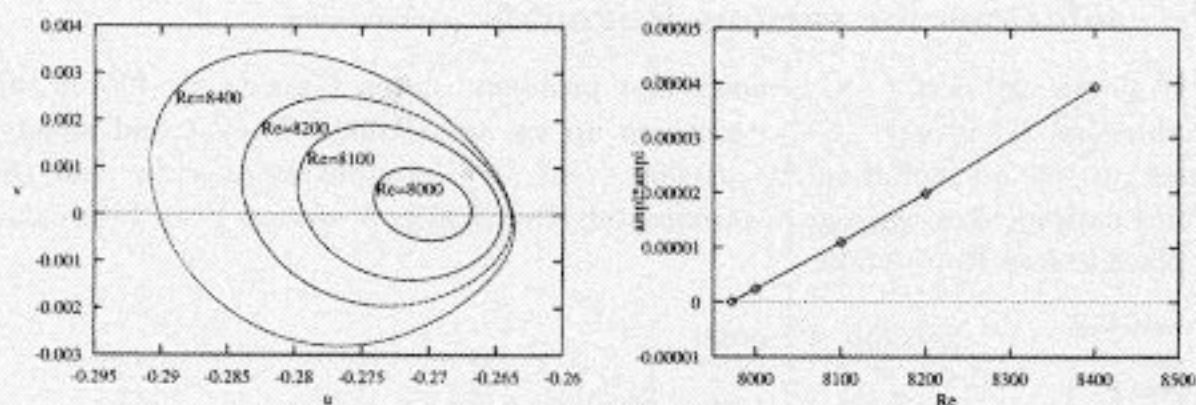


Figure 3.4: Phase plot of u versus v in $(0.5, 0.02)$ (left) and a plot of the squared amplitude of $v(0.5, 0.02)$ versus the Reynolds number.

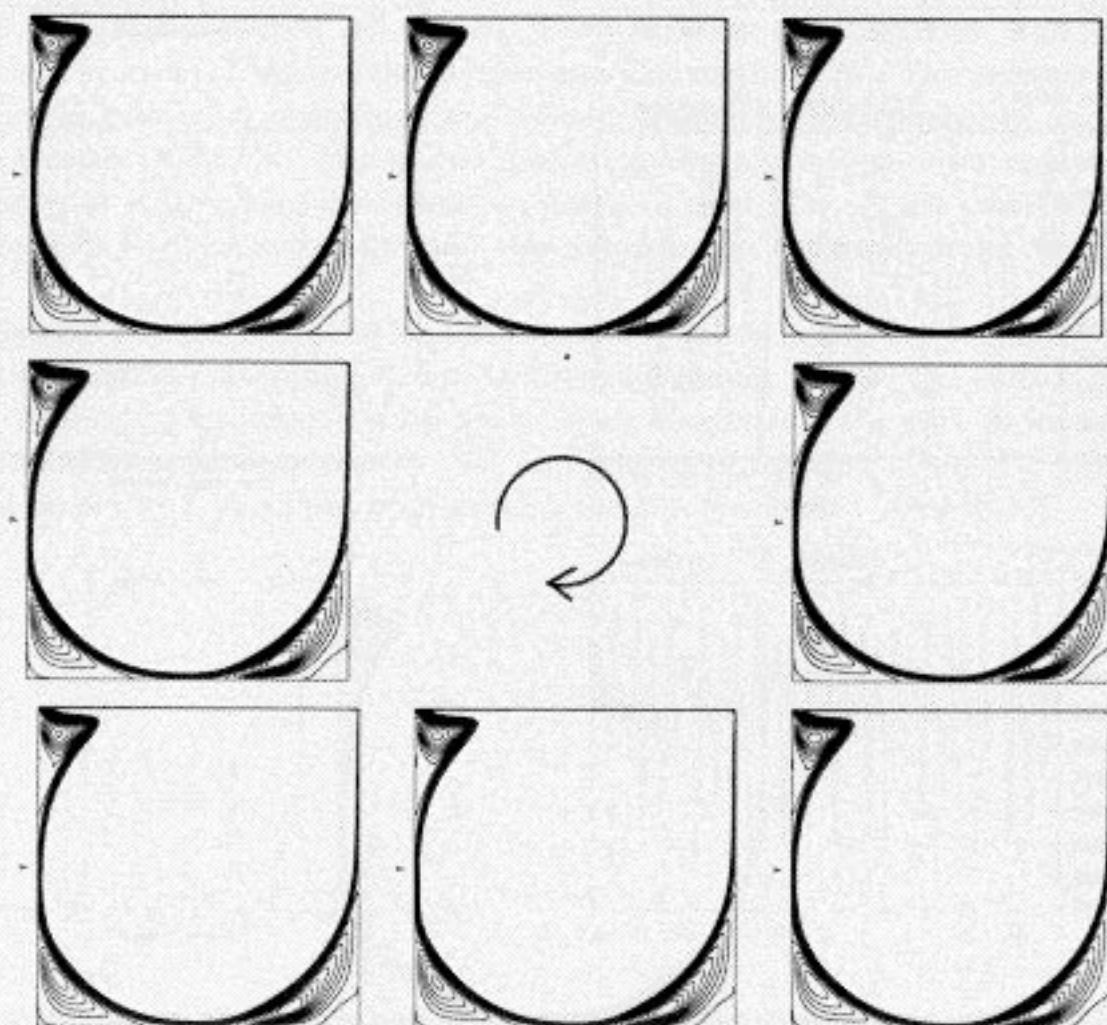


Figure 3.5: Streaklines of one period of the periodic solution at $Re = 8,000$.

To verify the solution at $Re=10,000$ we used 2 grids for the fourth-order accurate space discretization: a 250×250 grid and a 500×500 grid, both of which are slightly stretched. Further a second-order accurate discretization with a 333×333 uniform grid has been used. The three computed time-series of the total energy and the amplitude spectrum are shown in Fig. 3.3. All the simulations reached a solution with approximately the same 2 fundamental frequencies f_1 and f_2 . The other peaks in the amplitude spectrum are sub-harmonics, i.e. integer linear combinations of the two fundamental frequencies. The energy levels are not exactly the same. This might be due to different effective Reynolds numbers caused by the different level of numerical dissipation in the simulations, and/or by the way in which the energy is computed from the DNS data. Since the average total energy decreases if the Reynolds number increases, the first explanation would support the idea that the fourth-order method on the 500×500 grid has the smallest numerical dissipation.

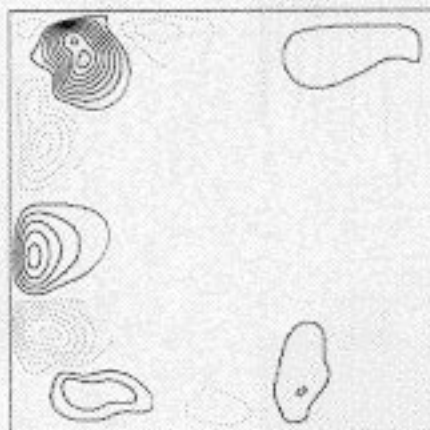


Figure 3.6: *streaklines of the deviation of the mean flow for the upper left plot of Fig. 3.5.*

The fourth-order accurate space discretization with a 250×250 grid is the cheapest, so we used this discretization and grid to do the other simulations. At $Re=6,000$ the solution is steady, and streamlines of the solutions are shown in Fig. 3.2. At $Re=8,000$ the solution is periodic, indicating that a Hopf bifurcation has taken place. It is known for the Hopf bifurcation (see [35]) that the amplitude of the solution grows (in first-order approximation) with the square-root of the bifurcation parameter. In our case, this means that the square of a velocity component should be proportional to $Re - Re_{critical}$ after the bifurcation. To verify this we performed simulations at Reynolds numbers 8,100, 8,200 and 8,400. A phase plot of $u(0.5, 0.02)$ against $v(0.5, 0.02)$ is shown in Fig. 3.4. The plot of the square of the v amplitude versus the Reynolds number is approximately a straight line. This line can be extrapolated to where it crosses the zero axis to approximate the bifurcation point, which gives a critical value of approximately $Re=7,972$. The period of the periodic solution after the bifurcation is 2.2 time unit.

The periodic solution at $Re = 8,000$ is shown in Fig. 3.5. In the lower left corner an eddy is oscillating. In the lower right corner no variation is visible. In the upper left corner the lower streakline is contracted and the eddy is oscillating.

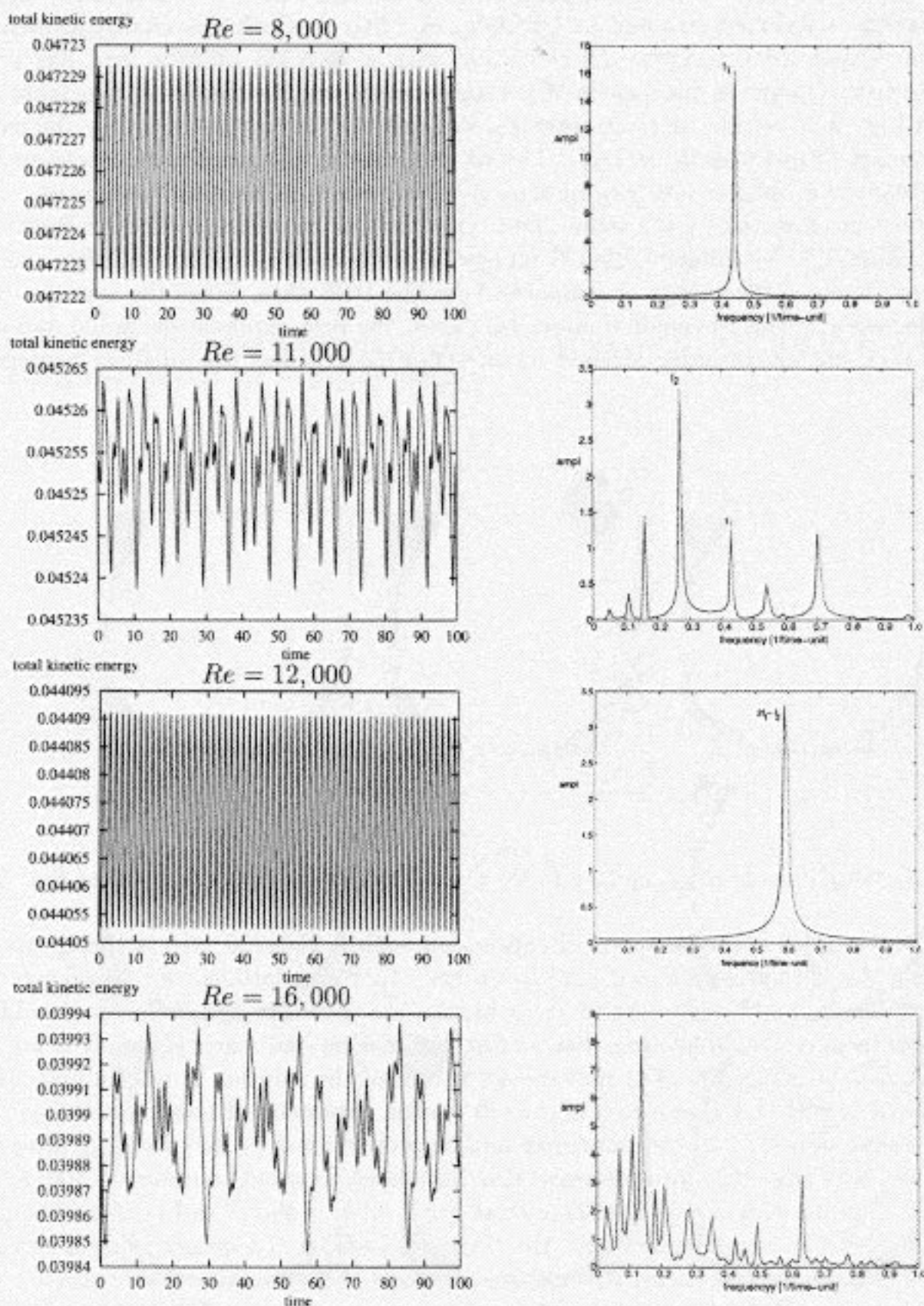


Figure 3.7: Time-series of the total energy (left) and amplitude spectrum (right) of simulations at $Re=8,000$, $Re=11,000$, $Re=12,000$, and $Re=16,000$.

When we look at the deviation from the mean flow in Fig 3.6 we see that the largest velocity fluctuations occur in the upper left corner, and some kind of vortex-street develops upstream.

When we increase the Reynolds number from 8,000 to 9,500 we still have a periodic solution with frequency f_1 . At Reynolds number 10,000 the computed solution has a second frequency as we have seen in Fig. 3.3. If we further increase the Reynolds number to 11,000 we find the same two fundamental frequencies (see Fig. 3.7) f_1 and f_2 as at $Re=10,000$. At Reynolds number 12,000 we find two different periodic solutions with frequencies which are subharmonics of the solution at $Re=11,000$, namely $2f_1 - f_2$ (see Fig. 3.7), and $f_1 + f_2$. The periodic solution with frequency $2f_1 - f_2$ is shown in Fig. 3.8. We can see that in the lower-left corner eddies are moving along the boundary of the large eddy in the core of the cavity. In between the eddies the streamlines enter the lower-left corner. In the upper-left corner an eddy is incorporated in the larger eddy every period. In the lower-right corner two eddies are merging.

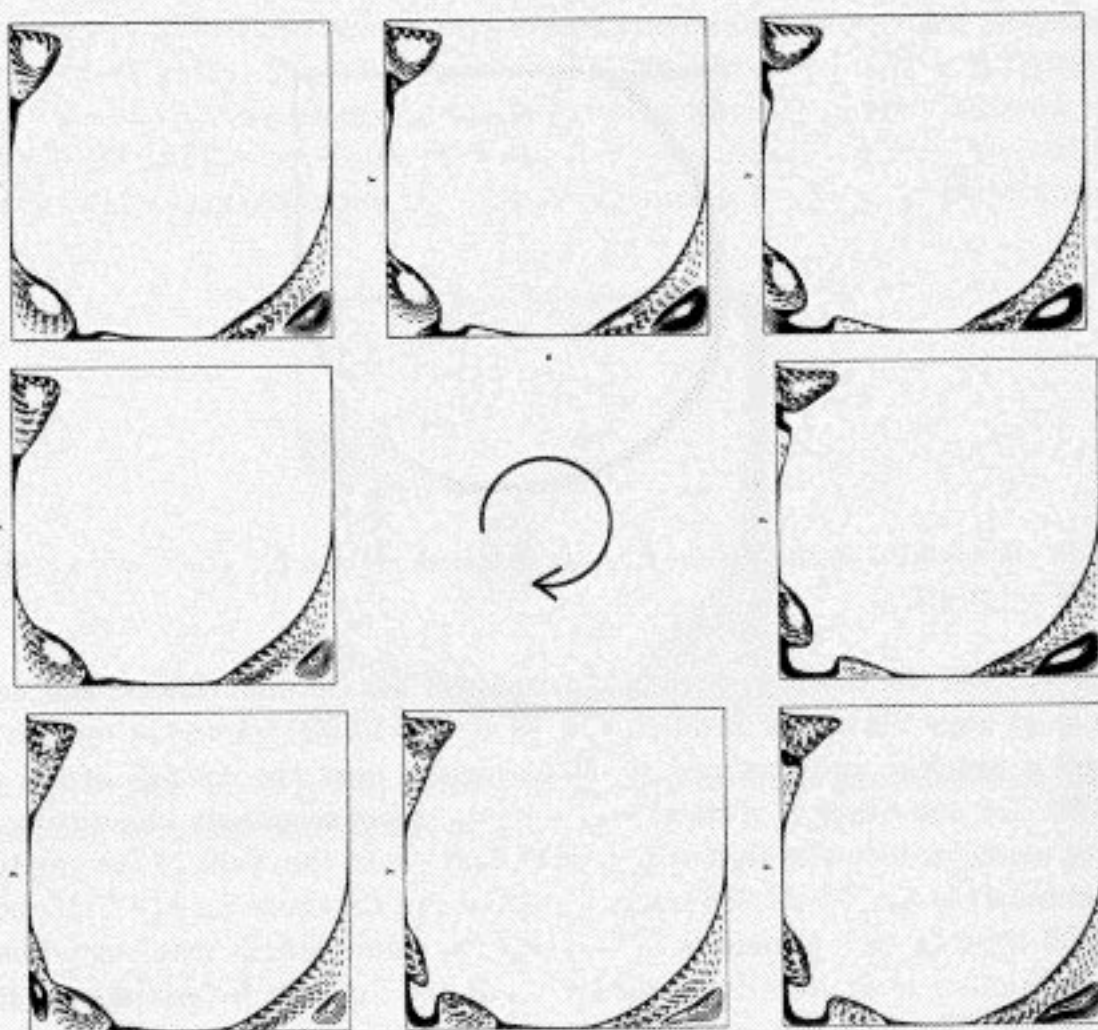


Figure 3.8: *Streaklines of one period of the periodic solution at $Re = 12,000$. Solid lines indicate a clock-wise rotation, and dashed lines indicate counter clock-wise rotation*

We computed solutions with the frequency $2f_1 - f_2$ at Reynolds numbers 12,000, 14,000, 15,000, and 16,000, and solutions with frequency $f_1 + f_2$ at Reynolds numbers 12,000 and 13,000. So, we expect that there are at least 2 stable periodic solutions for

these Reynolds numbers. The frequencies decrease a bit if we increase the Reynolds number somewhat. At $Re=16,000$ we found also another solution shown in Fig. 3.7. This solution has at least two different frequencies.

For the transition we can conclude that we found a first (Hopf) bifurcation at $Re=7,972$, a second instability with frequency f_2 between $Re = 9,500$ and $Re=10,000$, at least two (stable) periodic solutions at $Re=12,000$, also (stable) periodic solutions at $Re=13,000$ to $Re=16,000$, and at $Re=16,000$ also a solution with at least 2 different frequencies.

3.2.3 Simulation at $Re=22,000$

The database of flow-fields which we used to compute the POD (see Chapter 4) originates from a simulation at $Re=22,000$. We used this Reynolds number because we know, from previous computations, that the flow is turbulent at $Re=22,000$. Fig. 3.9 shows a snapshot of the flow in the driven cavity at $Re=22,000$. It takes roughly 5 non-dimensional time units for the core to turn around. We call this period a large-eddy turnover-time.

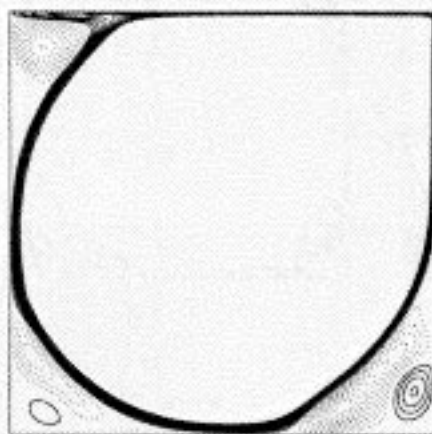


Figure 3.9: *Streaklines of the mean flow, as obtained from a 2D DNS of a lid-driven cavity flow at $Re = 22,000$.*

At $Re=22,000$ the motion of vortical structures has become chaotic and not confined in space as at lower Reynolds number, e.g. as at $Re=12,000$ where the motion of vortical structures is periodic and confined to small regions near the corners of the cavity. At $Re=22,000$ one can observe vortical structures moving seemingly chaotically around in the cavity along trajectories that stay relatively close to the walls of the cavity.

The simulation at $Re=22,000$ which supplied the database for the POD of chapter 4 lasted 3500 time units. It consists of two separate simulations that start from different initial conditions. Both start from earlier computed velocity fields that are statistically in equilibrium. The first run covers 500 time units; the second one last six times longer. So, in total, 700 large-eddy turnover-times have been computed. The energy (defined as $\int u^2 + v^2$) as obtained from both runs is shown in Fig. 3.10 (left). The first 500 time units correspond to the first run; the rest (from 500 to 3500 time units) belongs to the second run. The fluctuating energy of both runs is shown in Fig. 3.10 (right). The fluctuating energy is approximately 1.2 % of the total energy. One can observe two sharp peaks in the fluctuating energy and two deep valleys in the energy at ± 2300 time units and at

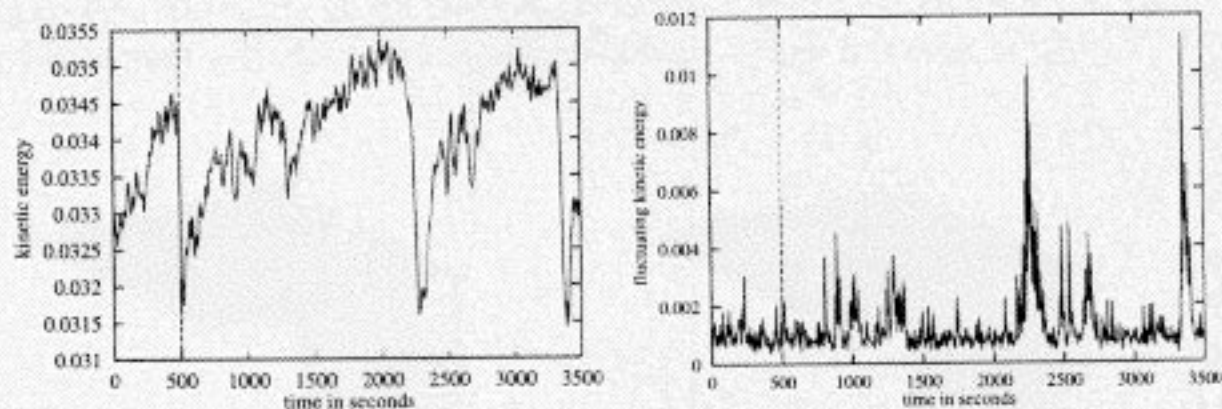


Figure 3.10: *The total energy (left) and the fluctuating energy (right) of 2D driven cavity ($Re=22,000$). After the first 500 time units the computation started from a new initial condition.*

± 3400 time units. These extremely rare events correspond to an eddy penetrating the core region of the cavity. Fig. 3.11 catches such an intruder in the act. Afterwards it dissipates. The fluctuating energy is relatively large when the core is altered, since the flow pattern is fairly different from the mean flow then. It is to be emphasized that Fig. 3.11 shows a rarity: this has happened only twice during 700 large-eddy turnover-times.

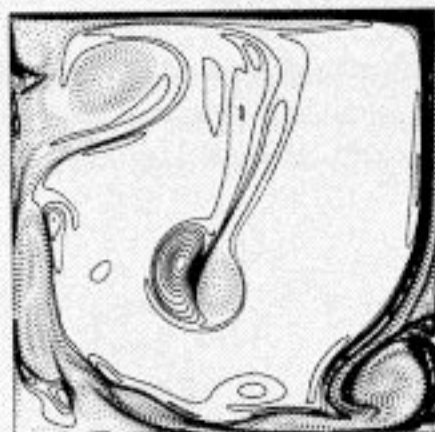


Figure 3.11: *A rarity: an eddy has penetrated the core region of the lid-driven cavity. This figure shows the vorticity; $Re=22,000$.*

3.3 3D DNS

3.3.1 Numerical method

The dimensions of the 3D driven cavity are $1 \times 1 \times 1$, and the computational grid has 100^3 cells. The grid is slightly stretched to get a fine grid near the walls. At the walls no-slip boundary conditions are imposed; the wall at $y=1$ is moving with unit velocity in the positive x -direction (as indicated in Fig. 3.12).

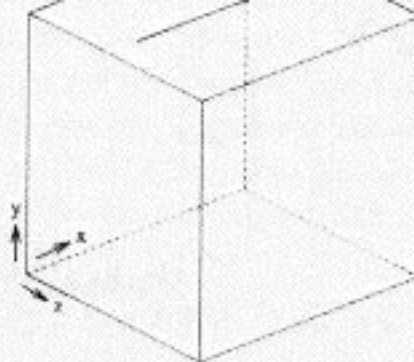


Figure 3.12: *Geometry of the 3D driven cavity with orientation.*

The equations (3.1) are discretized in space on a staggered grid using the Marker-and-Cell method. For the time integration of the convective term a two stage Adams-Bashforth method is used and for the diffusive term Euler integration. The Poisson equation for the pressure is solved by the conjugate gradient method with modified incomplete Choleski preconditioner. The preconditioner is modified according to Gustafson. The CPU-time for the numerical solution of the Navier-Stokes equation is $0.6\mu s$ per grid-point and time step on one processor of NLR's NEC-SX3. Details can be found in [58].

3.3.2 Simulation at $Re=10,000$

The code has been validated using the experimental data of Prasad and Koseff [42] (for $Re=10,000$). The mean flow and second order statistics have been compared, and they agreed well, indicating that the grid of 100^3 cells is fine enough for an accurate solution (see [58]).

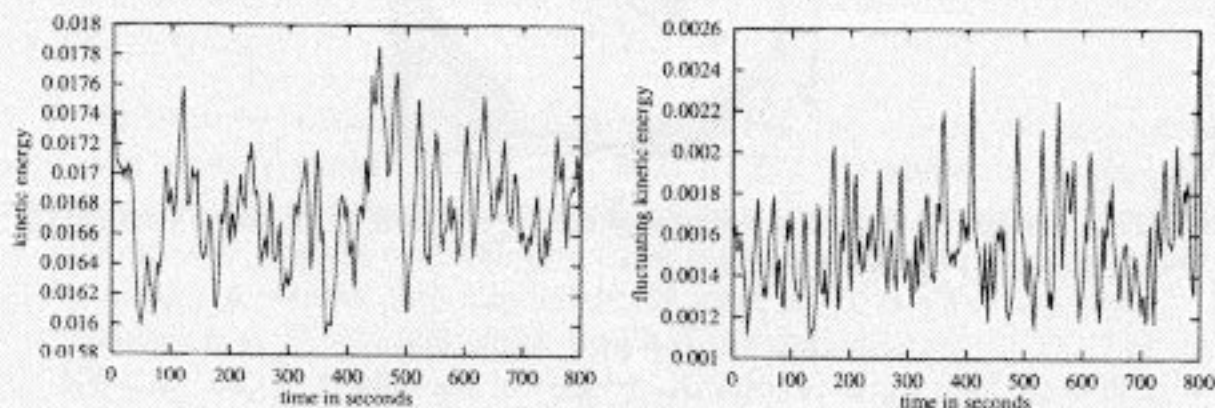


Figure 3.13: *The energy (left) and fluctuating energy (right) as obtained with the 3D DNS. This DNS provides data for the POD.*

The simulation from which we have extracted the data for the POD lasted 800 time units. The simulation started from a velocity field which was in statistical equilibrium. The energy, and the fluctuating energy during that simulation are shown in Fig. 3.13. We can see the 2D and 3D results differ. In the 3D case we did not observe a sudden

drop in energy. The average energy (defined by $\int u^2 + v^2 + w^2$) is 0.0168, and the energy of the fluctuations is 0.00155, that is approximately 9% of the total energy.

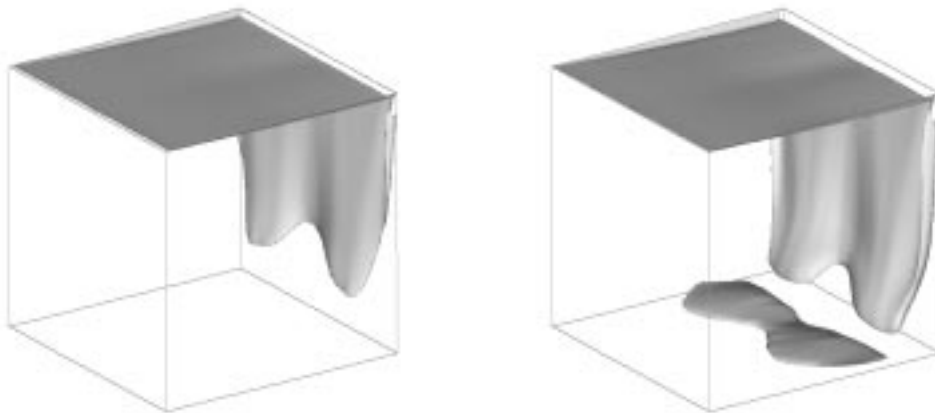


Figure 3.14: *Iso-energy surfaces of the mean flow.*

The data which we have used for the POD consisted of 320 snapshots of the velocity field, each 2.5 time units apart. When we compare the results of the dynamical system of chapter 6 with the experimental data of Prasad, the best result we can expect is to reproduce the data of these 320 snapshots. Therefore, we compared the mean velocity, Reynolds shear stress, and root-mean-square of velocity fluctuations, of the 320 snapshots with the experimental data of Prasad. The results are shown in Fig. 3.15. The figure shows a fairly good agreement between the DNS-data and the experiment. The difference between the whole data-set of the DNS and the 320 snapshots is fairly small.